Acta Mechanica Sinica
https://doi.org/10.1007/s10409-018-0806-8

RESEARCH PAPER

# Spectral measurements of hypervelocity flow in an expansion tunnel

**C. K. Yuan**[1,2] · **K. Zhou**[3] · **Y. F. Liu**[1,2] · **Z. M. Hu**[1,2] · **Z. L. Jiang**[1,2]

Received: 22 May 2018 / Revised: 31 July 2018 / Accepted: 1 August 2018

**Abstract**

Atmospheric reentry vehicles and planetary probes fly through the atmosphere at hypervelocity speed. At such speed, there is a significant proportion of heat load to the vehicle surface due to radiative heating. Accurate prediction needs a good knowledge of the radiation spectrum properties. In this paper, a high-speed camera and spectrograph coupled to an intensified charge-coupled device have been implemented to investigate the radiation flow over a semi-cylinder model. The experiments were carried out in the JF16 expansion tunnel with secondary shock velocity of 7.9 km·s$^{-1}$. Results show that the emission spectrum comprises several atomic lines and molecular band systems. We give detailed data of the radiation spectrum, shock shape, shock detached distance and radiation intensity varying with space and wavelength. This valuable experimental dataset will be helpful to validate computational fluid dynamics codes and radiation models, which equates to increased prediction accuracy of radiation heating. Also, some suggestions for spectral measurement in hypervelocity flow field were list in the end.

**Keywords** Spectral measurement · Hypervelocity flow · Radiation · Expansion tunnel

## 1 Introduction

Interest in atmospheric reentry vehicles and planetary probes has initiated studies of the aerothermal environments produced around the vehicles [1]. During this final phase of the mission, the vehicle flies through the atmosphere at hypervelocity speed, requiring that the heat shield must endure extreme thermal loading. At such speed, a significant proportion of the heat load is due to radiative heating. For example, on reentry from the moon, shock layer radiation constitutes 30–50% of the total surface heat flux in the peak heating region of the entry trajectory [2–4]. Velocities for aerocapture missions to Mars are estimated to be between 6.0 and 8.6 km·s$^{-1}$, with radiation contributing at least 80% of the incident heat flux at velocity over 8.5 km·s$^{-1}$ [5]. The peak radiative heat flux for the Pioneer Venus mission probes was predicted to be about half of the total heat flux [6]. Radiative heating is a complex phenomenon, and accurate estimates of heat transfer are dependent on good knowledge of the species present in the flow, the energy levels of the radiating species, the flow conditions and relevant thermochemical conditions, spectral range and resolution, spatial and temporal resolution, and radiation angle [7,8]. In the past, many radiation transport codes have been proposed, such as NEQAIR [9], Specair [10] and HARA [11]. But comparisons of experimental data with prediction of the models, have indicated evident difference [1]. As outlined by Johnston and Kleb [12], NASA's HARA radiation modeling code has an uncertainty of ±30%. The great uncertainties, predominantly due to the lack of experimental data, require large design margins, which equates to increased risk and/or heat shield mass [13–15].

The purpose of this work is to carry out experiments with representative reentry conditions and obtain radiance data over a large wavelength range for the validation of radiation models. Much research has been carried out with nonequilibrium gas downstream of the moving one-dimensional shock wave. It is only an analogy to the reentry condition. In this paper, a test model was placed in a hypervelocity flow, considering the flow divergence term and the boundary layer on the vehicle surface. In this configuration, a better understand-

✉ C. K. Yuan
yuanck@imech.ac.cn

1 State Key Laboratory of High-Temperature Gas Dynamic, Institute of Mechanics, Chinese Academy of Sciences, Beijing 100190, China

2 School of Engineering Sciences, University of Chinese Academy of Sciences, Beijing 100049, China

3 China Academy of Aerospace Aerodynamics, Beijing 100074, China

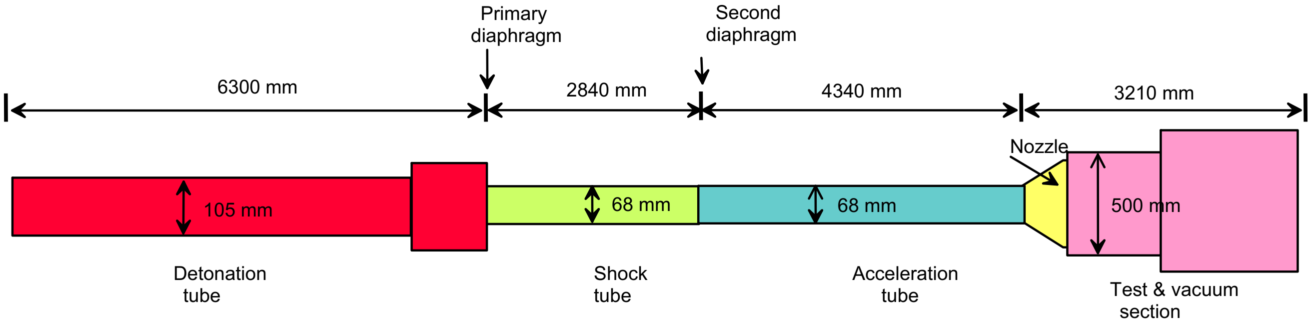

**Fig. 1** Schematic diagram of the detonation-driven expansion tunnel, JF16

ing of the measurement results rely on a good knowledge of radiation angle, flow structure and its relevant thermochemical conditions. This requires effective computational fluid dynamics (CFD) codes for hypervelocity. Detail data of shockwaves in hypervelocity flow are also given, which is helpful to validate the CFD codes.

## 2 Facility description

### 2.1 Expansion tunnel

Experiments were performed in the JF16 detonation-driven expansion tunnel capable of producing flows at velocities and pressures representative of entry trajectories. The upper limit of shock speed that can be produced is 10.2 km·s$^{-1}$. A schematic diagram is shown in Fig. 1, consisting of six main parts: the forward detonation cavity detonation tube, shock tube, acceleration tube, nozzle, test section, and vacuum section [16]. The facility is driven by a hydrogen/oxygen mixture filled in the detonation tube. Molar ratio of the mixture is determined by the given experimental situation. An igniter is installed at the left end of the detonation tube to initiate directly forward-running detonation. The scored steel primary diaphragm between the detonation and shock tube bursts after the arrival of the detonation wave, at the same time launching a shock into the shock tube containing the test gas at low pressure. The high pressure shock accelerates through the second mylar diaphragm into the acceleration tube, where the test gas is further accelerated by an unsteady expansion wave. The nozzle with aero ratio of 16 enlarges the core flowfield at the nozzle exit to approximately 174 mm. Piezoelectric sensors are flush-mounted along the shock tube and the acceleration tube, recording the static pressure histories. Shock speed is calculated by the method of time of flight. Summary of the initial fill conditions and freestream conditions for this series experiment are shown in Table 1. Freestream parameters were calculated using the method introduced in Ref. [17].

**Table 1** Initial fill conditions and freestream conditions for this series experiment

| | |
|---|---|
| Fill condition | |
| Detonation driver (MPa) | 1.0, 75%$H_2$ +25%$O_2$ |
| Shock tube (kPa) | 3.0, air |
| Acceleration tube (Pa) | 20, air |
| Test and vacuum section (Pa) | 20, air |
| Diaphragm | |
| Primary diaphragm (mm) | 2, mild steel |
| Second diaphragm (mm) | 0.15, mylar |
| Shock speed (measured) | |
| First shock velocity (m·s$^{-1}$) | 4762 |
| Secondary shock velocity (m·s$^{-1}$) | 7907 |
| Freestream (calculated) | |
| Static temperature (K) | 956 |
| Static pressure (Pa) | 195 |
| Density (kg·m$^{-3}$) | 0.0006 |
| Mach number | 12 |

### 2.2 Instrumentation

The model is a 51.2 mm diameter semi-cylinder that is 50 mm in length, located 10 mm downstream of the nozzle exit. The use of such a shape results in increased optical signal on the detector by integrating along its entire length.

The optical diagnostic system consists of two parts: the flow visualization system and spectral emission measurements system. A schematic representation of the optical layout is shown in Fig. 2. Flow visualization was carried out with an SA4 high-speed colour camera taking photographs from the test section side optical windows, its exposure time is set to be 1 μs, and time interval between successive frames is 33 μs.

The spectral emission measurements system capable of recording spatially and spectrally resolved image at a single instant. It includes a spectrometer, manufactured by Andor, with 500 mm focal length and 150 lines, 600 lines, or 1200

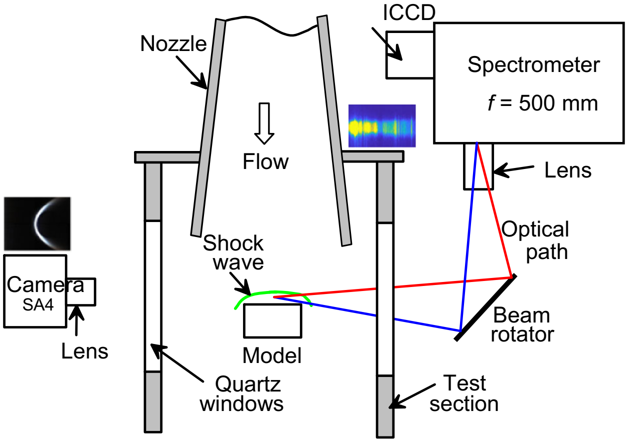

**Fig. 2** Schematic of optical layout

**Table 2** Specifications of the spectrometer and ICCD camera

| | |
|---|---|
| Spectrometer | |
| Model | Andor, Shamrock 500i |
| Focal length (mm) | 500 |
| $f/\#$ | 6.5 |
| Magnification | 1 |
| Grating | |
| Lines ($mm^{-1}$) | 150 |
| Blaze wavelength (nm) | 800 |
| Nominal dispersion ($nm \cdot mm^{-1}$) | 12.83 |
| Resolution (nm) | 0.52 |
| ICCD | |
| Model | Andor, iStar 334T |
| Spectral range (nm) | 120–1100 |
| Active pixels | $1024 \times 1024$ |
| Effective pixel size ($\mu m$) | $13 \times 13$ |

lines per millimeter grating. Output plane of the spectrometer was coupled to an intensified charge-coupled device (ICCD) camera. Detail specifications of the spectrometer and ICCD camera are listed in Table 2.

All measurements are taken with a 150 lines per millimeter grating, 50 $\mu$m entrance slit and 1 $\mu$s gate width over a range of different central wavelengths covering the full region from 398 nm to 886 nm. The separately acquired spectra covering 170 nm each are concatenated during post-processing to give the full spectrum. Using a Nikon zoom lens, region along the flow stagnation streamline in front of the cylinder was focused onto the spectrometer entrance slit. As the entrance slit on the spectrometer is vertical and the flow stagnation streamline is horizontal, a beam rotator was used in the system to allow spatial resolution along the direction of interest. Details of optical path is shown in Table 3.

**Table 3** Details of optical path

| | |
|---|---|
| Focusing mirror to model centerline (mm) | 1735 |
| Focusing mirror to slit (mm) | 95 |
| Total optical path (mm) | 1830 |
| Focal length (mm) | 90 |
| $f$-number | 2.5 |
| Aperture (mm) | 36 |
| Magnification | 0.055 |
| Depth of field (mm) | 50 |
| Calculated circle of confusion (mm) | 0.028 |

The ICCD and high-speed camera were triggered from a piezoelectric sensor flush-mounted in the entrance of the nozzle with a delay to ensure measurements were taken during the effective test time.

### 2.3 Calibration

The optical diagnostic system was calibrated to enable comparison with numerical simulations. Wavelength calibration is accomplished using Hg lamp with a known spectral radiance. The spatial dimension was calibrated by imaging a ruled grid placed in the object plane.

## 3 Results and discussion

### 3.1 Evaluation of the effective test time

Figure 3 shows the wall pressure history measured at the entrance of the nozzle. The sharp jump stands for the arrival of the incident shock. It is observed that the pressure behind the sharp jump keeps an almost constant value for about 100 $\mu$s and then gradually increases. Actually, the pressure plateau does not provide sufficient information to determine the uniform test duration. It is also difficult to quantify accurately the test time using only conventional techniques such as pitot pressure measurements [18]. Flow emission characters will be helpful to further diagnose the flow state. So, flow visualization experiments were carried out to further identify the effective test time.

Photographs taken by the high speed camera are shown in Fig. 4 where the time interval between successive frames is 33 $\mu$s. Figure 4a is the first image after the gas flow reach the model. From Fig. 4c, d, we can see that color of the right side of the image change form bright white to orange, and the orange area increases with test time in Fig. 4e, f. This fact indicated that the effective test time is no less than 66 $\mu$s and no more than 99 $\mu$s. One thing to note here is that the shock layer in Fig. 4a appears to be light blue is because of the flow field around the test model has not reached a quasi-

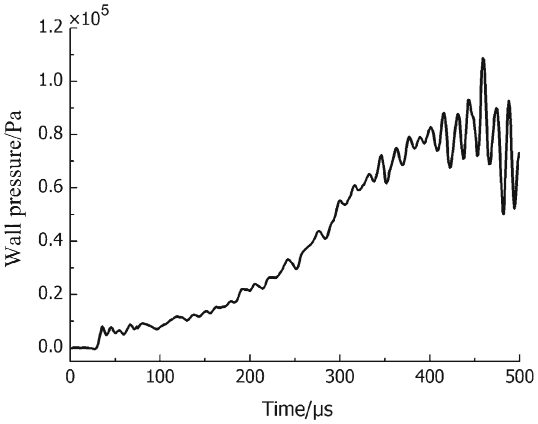

**Fig. 3** Wall pressure history measured at the nozzle entrance

steady state. Care should be taken while selecting model size, for more test time will be consumed with a larger model size. In our experiments the time taken to reach the steady state of such a model is about 33 μs. Based on this analysis, spectral emission measurements will be carried out 60 μs after the hypervelocity flow arrives at the model, just before the imaging time of Fig. 4c. This ensures that experiments were carried out in the effective time of the expansion tunnel and flow field around the model is stable.

### 3.2 Shock detached distance

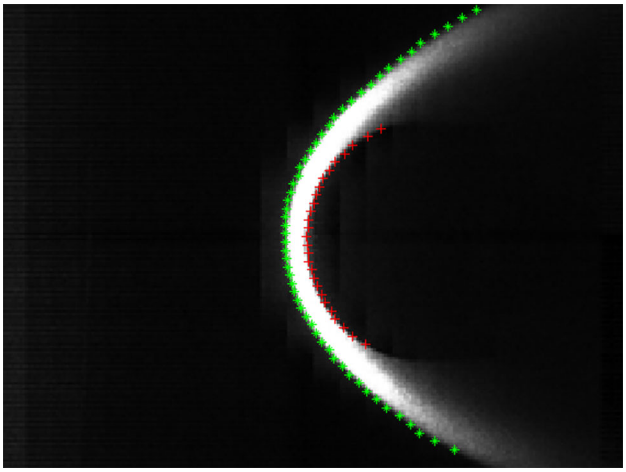

**Fig. 5** Typical result of the imaging processing algorithm

In the present paper, the thickness of the radiating layer, approximately equal to the shock detached distance [18], is an important characteristic parameter. Figure 4 was further analyzed with a MATLAB imaging processing algorithm to extract the shockwave position. Typical processing result was shown in Fig. 5, where star dots stand for the shockwave and cross dots represent the test model surface.

Positions of the shockwave and test model surface were accurately identified. Detail processing results of Fig. 4a–d are shown in Fig. 6 and the Appendix A1, which are helpful to verify CFD simulation results and improve its accuracy. Shock detached distance was normalized by model diameter for further comparison. Normalized shock detached distance along the stagnation line of the test gas (17.96%) is slightly

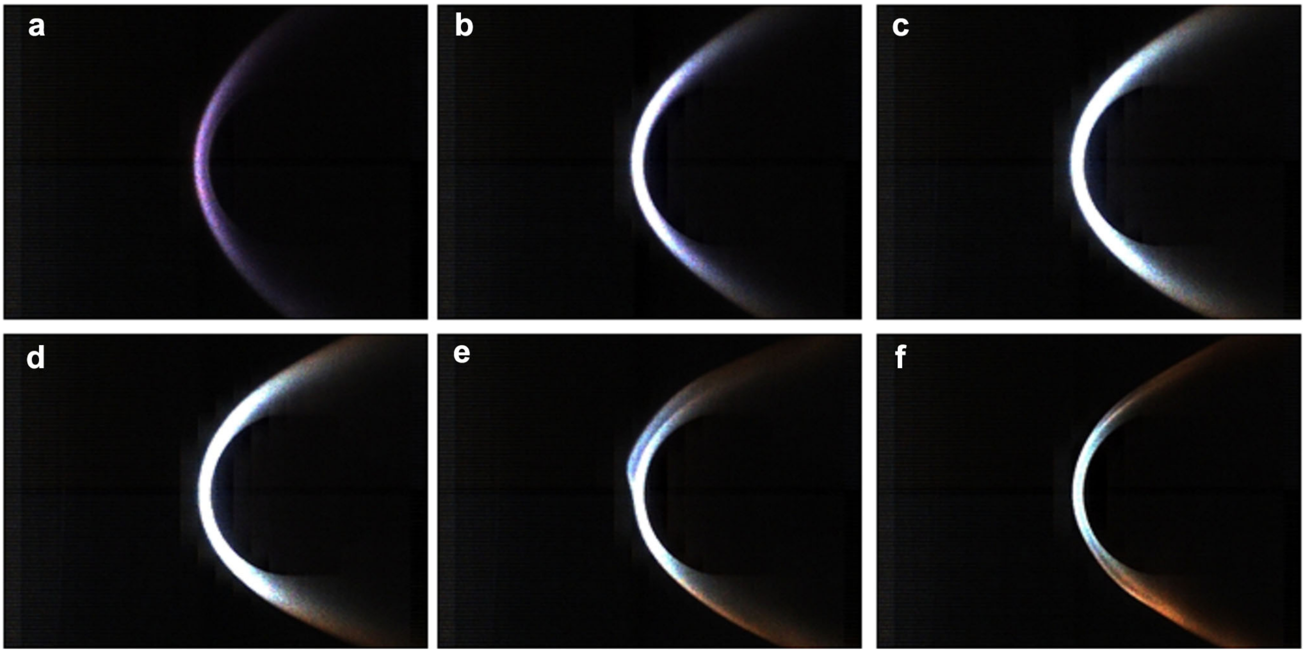

**Fig. 4** Photos of the shock over the cylinder in the flow of 7.9 km·s$^{-1}$, the time interval is 33 μs and the exposure time is 1 μs. **a** $t = 0$ μs. **b** $t = 33$ μs. **c** $t = 66$ μs. **d** $t = 99$ μs. **e** $t = 132$ μs. **f** $t = 165$ μs

greater than that of the driver gas (13.98%). This decrease is caused by an increase in the driver gas flow Mach number. As we can see from Fig. 6, the shock shape is more sensitive to the flow state than shock detached distance. Therefore, it is more effective to evaluate numerical simulation results by shock wave shape.

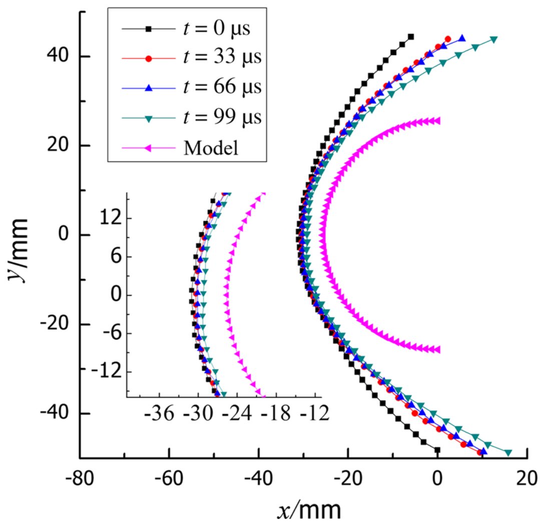

**Fig. 6** Processing results of shockwave position

## 3.3 Radiation spectrum properties

Radiation spectra of air under the test conditions are shown in Fig. 7 from three tests with different grating central wavelengths at the same nominal condition. Spectrometer configurations overlap each other to ensure continuous coverage from 398 to 886 nm. Background radiation produced due to thermal and electronic noise was removed by subtracting a dark image taken just before the begining of the experiment. In Fig. 7, the vertical axis shows the distance along

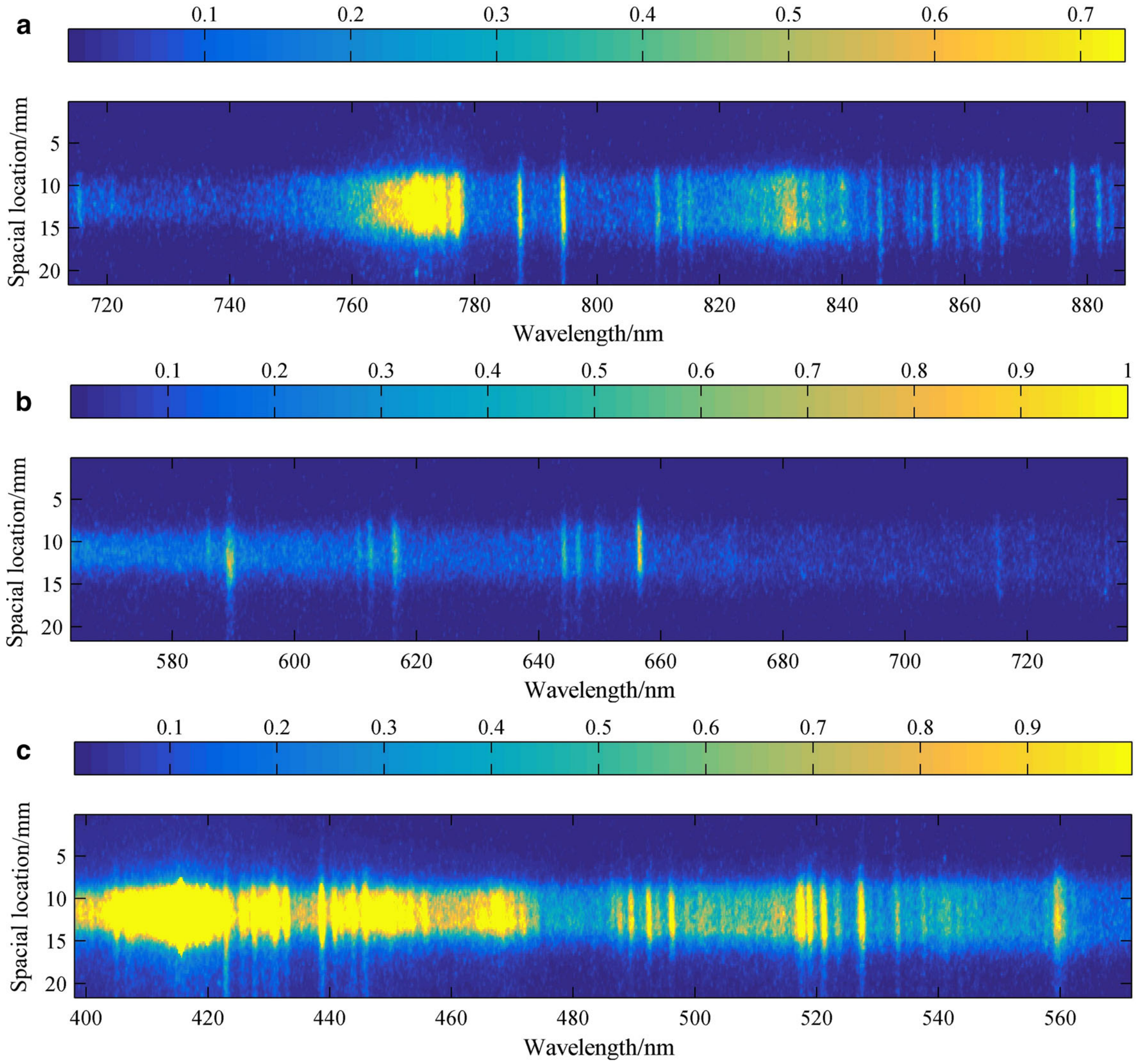

**Fig. 7** Image of the normalized spectral radiance measured with different grating central wavelengths. **a** 800 nm. **b** 650 nm. **c** 485 nm

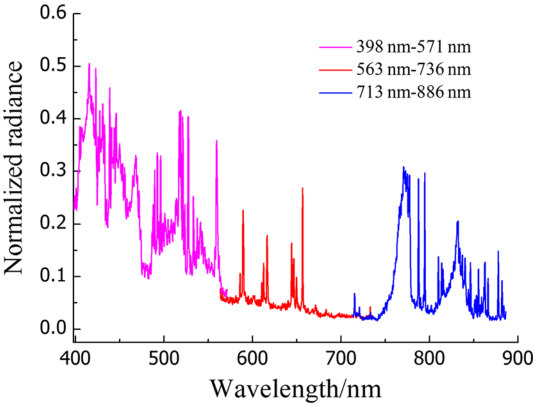

**Fig. 8** Spatially integrated spectrum of the shock emission

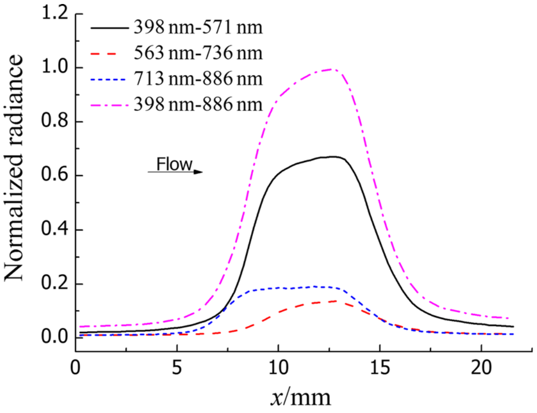

**Fig. 9** Radiation along the direction of flow

the stagnation streamline while the horizontal axis shows the wavelength. Orientation of each image is such that the free stream flow is from top to bottom in the image. To compare radiation intensities at different wavelengths, radiation intensity has been normalized to the peak value, considering the varying quantum efficiency of ICCD camera and grating efficiency with wavelength. Pseudo-color treatment technique was used, so the shock layer in front of the model is easily identified by the onset of bright yellow zones.

The spectral radiance is integrated over the spatial direction to inspect the major emission features present at the test condition. This also provides a high signal-to-noise ratio. As shown in Fig. 8, it makes clear that spectrum of the shock emission comprise several atomic lines and molecular band systems. Detailed interpretation of the spectral data still needs further study.

The spectrum shown in Fig. 7 has also been integrated over wavelengths. Figure 9 is the resulting normalized radiance plotted as a function of position and the free stream flow is from left to right in the image.

Different from the high speed camera results shown in Fig. 4, neither the shock nor the test model appears as a sharp jump in Fig. 7. The reasons for the slow rise and fall of the radiation intensity were difficult to pinpoint. From an experimental point of view, there may be three reasons. Firstly, although with careful calibration, axis of the test model may have included angle with the spectrometer optical axis. So, the spectral image may be a projection along the optical axis direction, changing the actual size of the imaging objects. Secondly, it may partially be attributed to radiation from flow spilling around the side of the model for the relative low aspect ratio. Finally, it may be caused by the reflection of the optical windows, test model surface and inner wall of the test section. Innovative experimental configurations are required to confirm the specific reason. The slow raise and fall of radiation makes it difficult to unify the $x$ axis starting point in the processing results of high-speed camera and ICCD. In the shock layer, radiation intensity gradually increases. This may be caused by the chemical reactions and radiation relaxation processes. Further research is needed to illustrate the phenomenon.

## 4 Conclusions

The methodology to conduct spectral measurements of hypervelocity in an expansion tunnel has been described. Wide spectral range radiation data were obtained with typical reentry conditions. Results show that emission spectra comprise several atomic lines and molecular band systems. Spectral measurement results still require comprehensive and detailed analysis. Meanwhile, data of shock shape, shock detached distance and radiation intensity varying with space and wavelength were given. This valuable experimental dataset will be used to validate CFD codes and radiation models.

Also, the conclusions are drawn as follows. (1) The radiation spectrum should be measured after the flow field around the test model has reached a quasi-steady state. For test time of the expansion tunnel is relatively short and a larger model consumes more test time, model size must be limited. (2) Shock shape is more sensitive to the flow state than shock detached distance. Therefore, it is more effective to evaluate numerical simulation results. (3) To configure a spectral measurement system, great care should be taken in the reflection of the optical windows, test model surface and inner wall of the test section.

**Acknowledgements** This work was supported by the National Natural Science Foundation of China (Grants 11602275, 11672308, 11672312, and 11532014.). The author thanks the people helping with this work and acknowledges the valuable suggestions from the peer reviewers.

# Appendix

## A1: Image processing results of the shock wave position

| $t$ = 0 µs (Fig. 4a) | | $t$ = 33 µs (Fig. 4b) | | $t$ = 99 µs (Fig. 4c) | | $t$ = 132 µs (Fig. 4d) | |
|---|---|---|---|---|---|---|---|
| $x$ (mm) | $y$ (mm) | $x$ (mm) | $y$ (mm) | $x$ (mm) | $y$ (mm) | $x$ (mm) | $y$ (mm) |
| −0.075 | −48.131 | 9.522 | −48.680 | 10.223 | −48.545 | 15.788 | −48.572 |
| −3.126 | −46.385 | 5.817 | −46.934 | 7.172 | −46.799 | 11.212 | −46.826 |
| −4.870 | −44.639 | 2.983 | −45.188 | 4.121 | −45.053 | 8.378 | −45.080 |
| −6.831 | −42.893 | 0.368 | −43.442 | 1.288 | −43.307 | 4.674 | −43.334 |
| −8.793 | −41.147 | −2.683 | −41.696 | −1.545 | −41.561 | 1.840 | −41.588 |
| −10.536 | −39.401 | −5.080 | −39.950 | −3.507 | −39.815 | −0.993 | −39.842 |
| −12.280 | −37.655 | −6.606 | −38.204 | −5.904 | −38.069 | −3.826 | −38.096 |
| −14.023 | −35.909 | −8.785 | −36.458 | −8.301 | −36.323 | −6.659 | −36.350 |
| −15.331 | −34.163 | −10.746 | −34.712 | −10.263 | −34.577 | −8.838 | −34.604 |
| −16.856 | −32.417 | −12.708 | −32.966 | −12.006 | −32.831 | −11.236 | −32.858 |
| −17.946 | −30.671 | −14.233 | −31.220 | −14.186 | −31.085 | −13.633 | −31.112 |
| −19.254 | −28.925 | −16.413 | −29.474 | −16.147 | −29.339 | −15.377 | −29.366 |
| −20.343 | −27.179 | −17.502 | −27.728 | −18.108 | −27.593 | −17.120 | −27.620 |
| −21.433 | −25.433 | −19.682 | −25.982 | −19.852 | −25.847 | −18.646 | −25.874 |
| −22.741 | −23.687 | −21.425 | −24.236 | −20.941 | −24.101 | −20.389 | −24.128 |
| −23.612 | −21.941 | −22.733 | −22.490 | −22.467 | −22.355 | −21.479 | −22.382 |
| −24.702 | −20.195 | −23.823 | −20.744 | −23.557 | −20.609 | −22.568 | −20.636 |
| −25.574 | −18.449 | −24.912 | −18.998 | −24.864 | −18.863 | −23.876 | −18.890 |
| −26.663 | −16.703 | −26.002 | −17.252 | −25.954 | −17.117 | −24.966 | −17.144 |
| −27.535 | −14.957 | −27.092 | −15.506 | −27.044 | −15.371 | −26.055 | −15.398 |
| −28.407 | −13.211 | −27.745 | −13.760 | −27.262 | −13.625 | −27.145 | −13.652 |
| −29.061 | −11.465 | −28.399 | −12.014 | −28.569 | −11.879 | −27.363 | −11.906 |
| −29.497 | −9.719 | −29.053 | −10.268 | −29.005 | −10.133 | −28.235 | −10.160 |
| −30.150 | −7.973 | −29.489 | −8.522 | −29.659 | −8.387 | −28.671 | −8.414 |
| −30.586 | −6.227 | −29.925 | −6.776 | −29.877 | −6.641 | −29.106 | −6.668 |
| −30.586 | −4.481 | −30.143 | −5.030 | −30.095 | −4.895 | −29.292 | −4.922 |
| −30.804 | −2.735 | −30.361 | −3.284 | −30.095 | −3.149 | −29.331 | −3.176 |
| −31.022 | −0.989 | −30.361 | −1.538 | −30.095 | −1.403 | −29.178 | −1.430 |
| −31.022 | 0.757 | −30.361 | 0.208 | −30.095 | 0.343 | −29.215 | 0.316 |
| −30.804 | 2.503 | −30.143 | 1.954 | −30.095 | 2.089 | −29.106 | 2.062 |
| −30.368 | 4.249 | −30.143 | 3.700 | −29.877 | 3.835 | −28.888 | 3.808 |
| −30.368 | 5.995 | −29.707 | 5.446 | −29.659 | 5.581 | −28.888 | 5.554 |
| −29.932 | 7.741 | −29.489 | 7.192 | −29.223 | 7.327 | −28.671 | 7.300 |
| −29.497 | 9.487 | −29.053 | 8.938 | −28.787 | 9.073 | −28.453 | 9.046 |
| −28.843 | 11.233 | −28.617 | 10.684 | −28.351 | 10.819 | −27.581 | 10.792 |
| −28.189 | 12.979 | −27.963 | 12.430 | −27.480 | 12.565 | −26.927 | 12.538 |
| −27.753 | 14.725 | −26.874 | 14.176 | −26.826 | 14.311 | −26.055 | 14.284 |
| −27.099 | 16.471 | −26.002 | 15.922 | −25.736 | 16.057 | −25.184 | 16.030 |
| −26.445 | 18.217 | −24.912 | 17.668 | −24.646 | 17.803 | −24.094 | 17.776 |
| −25.574 | 19.963 | −23.823 | 19.414 | −23.557 | 19.549 | −22.568 | 19.522 |
| −24.702 | 21.709 | −22.733 | 21.160 | −22.467 | 21.295 | −21.479 | 21.268 |
| −23.612 | 23.455 | −21.207 | 22.906 | −20.941 | 23.041 | −19.735 | 23.014 |
| −22.523 | 25.201 | −19.900 | 24.652 | −19.852 | 24.787 | −18.646 | 24.760 |
| −21.433 | 26.947 | −18.156 | 26.398 | −18.108 | 26.533 | −16.902 | 26.506 |
| −20.125 | 28.693 | −17.067 | 28.144 | −16.801 | 28.279 | −14.723 | 28.252 |
| −19.036 | 30.439 | −15.323 | 29.890 | −14.621 | 30.025 | −12.543 | 29.998 |
| −17.946 | 32.185 | −13.362 | 31.636 | −12.878 | 31.771 | −10.364 | 31.744 |
| −16.420 | 33.931 | −11.400 | 33.382 | −10.916 | 33.517 | −7.749 | 33.490 |
| −14.895 | 35.677 | −9.221 | 35.128 | −8.737 | 35.263 | −4.916 | 35.236 |
| −12.934 | 37.423 | −7.042 | 36.874 | −6.122 | 37.009 | −2.082 | 36.982 |
| −11.626 | 39.169 | −4.644 | 38.620 | −3.725 | 38.755 | 1.187 | 38.728 |
| −9.882 | 40.915 | −2.247 | 40.366 | −1.763 | 40.501 | 4.674 | 40.474 |
| −7.921 | 42.661 | 0.150 | 42.112 | 1.288 | 42.247 | 8.378 | 42.220 |
| −5.960 | 44.407 | 2.330 | 43.858 | 5.429 | 43.993 | 12.519 | 43.966 |

# References

1. Johnston, C.O., Hollis, B.R., Sutton, K.: Spectrum modeling for air shock-layer radiation at lunar-return conditions. J. Spacecr Rockets **45**, 865–878 (2008)
2. Grinstead, J.H., Wilder, M.C., Olejniczak, J.O., et al.: Shock-heated air radiation measurements at lunar return conditions. In: Proceedings of 46th AIAA Aerospace Sciences Meeting and Exhibit, Nevada, January 7–10 (2008)
3. Sheikh, U.A., Morgan, R.G., McIntyre, T.J., et al.: Through surface and across surface vacuum ultraviolet spectral measurements in an expansion tube. In: Proceedings of 44th AIAA Thermophysic Conference, San Diego, June 24–27 (2013)
4. Sheikh, U.A., Morgan, R.G., Zander, F., et al.: Vacuum ultraviolet emission spectroscopy system for superorbital re-entries. In: Proceedings of 18th AIAA/3AF International Space Planes and Hypersonic Systems and Technologies Conference, Tours, September 24–28 (2012)
5. Potter, D.F., Gollan, R.J., Eichmann, T., et al.: Simulation of $CO_2$–$N_2$ expansion tunnel flows for the study of radiating shock layers. In: Proceedings of 46th AIAA Aerospace Sciences Meeting and Exhibit, Nevada, January 7–10 (2008)
6. Grinstead, J.H., Wright, M.J., Bogdanoff, D.W., et al.: Shock radiation measurements for mars aerocapture radiative heating analysis. J. Thermophys. Heat Transf. **23**, 249–255 (2009)
7. Grinstead, J.H., Wilder, M.C., Reda, D.C., et al.: *Advanced Spectroscopic and Thermal Imaging Instrumentation for Shock Tube and Ballistic Range Facilities.* Technical Report (RTO, 2010)
8. Eichmann, T.N., Brandis, A., Potter, D., et al.: Radiating hypersonic flow studies using a super orbital expansion tube. In: Proceedings of 26th AIAA Aerodynamic Measurement Technology and Ground Testing Conference, Washington, June 23–36 (2008)
9. Whiting, E.E., Park, C., Liu, Y., et al.: NEQAIR96, Nonequilibrium and Equilibrium Radiative Transport and Spectra Program: User's Manual (1996)
10. Laux, C.O., Spence, T.G., Kruger, C.H., et al.: Optical diagnostics of atmospheric pressure air plasmas. Plasma Sources Sci. Technol. **12**, 125–138 (2003)
11. Johnston, C.O.: A comparison of EAST shock-tube radiation measurements with a new air radiation model. In: Proceedings of 46th AIAA Aerospace Sciences Meeting and Exhibit, Nevada, January 7–10 (2008)
12. Johnston, C.O., Kleb, B.: Uncertainty analysis of air radiation for lunar-return shock layers. J. Spacecr Rockets **49**, 425–434 (2012)

13. Parker, R., Dufrene, A., MacLean, M., et al.: Emission measurements from high enthalpy flow on a cylinder in the LENS-XX hypervelocity expansion tunnel. In: Proceedings of 51st AIAA Aerospace Sciences Meeting including the New Horizons Forum and Aerospace Exposition, Texas, January 7–10 (2013)
14. Bose, D., Wright, M.J., Bogdanoff, D.W., et al.: Modeling and experimental assessment of CN radiation behind a strong shock wave. J. Thermophys. Heat Transf. **20**, 220–230 (2006)
15. Sheikh, U.A., Morgan, R.G., McIntyre, T.J.: Vacuum ultraviolet spectral measurements for superorbital earth entry in X2 expansion tube mcintyre. AIAA J. **53**, 3589–3602 (2015)
16. Jiang, Z.L., Wu, B., Gao, Y.L., et al.: Development of the detonation-driven expansion tube for orbital speed experiments. Sci. China Technol. Sci. **58**, 695–700 (2015)
17. Hu, Z.M., Wang, C., Jiang, Z.L., et al.: On the numerical technique for the simulation of hypervelocity test flows. Comput. Fluids **106**, 12–18 (2015)
18. Sasoh, A., Ohnishi, Y., Ramjaun, D., et al.: Effective test time evaluation in high-enthalpy expansion tube. AIAA J. **39**, 2141–2147 (2001)